

AASERT Grant #N00014-93-1-0827

**Fifth Semi-Annual Progress Report**  
(covering the period of 07/26/95-02/15/96)

**Project Title: Investigation of Normal Incidence High-  
Performance P-type Strained Layer  
InGaAs/AlGaAs and GaAs/AlGaAs Quantum  
Well Infrared Photodetectors.**

Submitted to

Max N. Yoder

Office of Naval Research  
Code 3140  
800 North Quincy Street  
Arlington, VA 22217-5000

**DISTRIBUTION STATEMENT A**

**Approved for public release;  
Distribution Unlimited**

Prepared by

Jerome T. Chu  
Student

and

Sheng S. Li  
Professor

Department of Electrical Engineering  
University of Florida  
Gainesville, FL 32611

Tel. (904) 392-4937  
Fax (904) 392-8671  
E-mail: ShengLi@ENG.UFL.EDU

19960222 050

February 15, 1996

THIS DOCUMENT CONTAINS UNCLASSIFIED INFORMATION

REPORT DOCUMENTATION PAGE			Form Approved OMB No. 0704-0188	
<small>Public reporting burden for this collection of information is estimated to average 1 hour per response, including the time for reviewing instructions, searching existing data sources, gathering and maintaining the data needed, and completing and reviewing the collection of information. Send comments regarding this burden estimate or any other aspect of this collection of information, including suggestions for reducing this burden, to Washington Headquarters Services, Directorate for Information Operations and Reports, 1215 Jefferson Davis Highway, Suite 1204, Arlington, VA 22202-4302, and to the Office of Management and Budget, Paperwork Reduction Project (0704-0188), Washington, DC 20503.</small>				
1. AGENCY USE ONLY (Leave blank)	2. REPORT DATE 15 February 1996	3. REPORT TYPE AND DATES COVERED Progress Report: 07/26/95-02/15/96		
4. TITLE AND SUBTITLE Investigation of Normal Incident High Performance P-type Strained Layer InGaAs/AlGaAs and GaAs/AlGaAs QWIPs		5. FUNDING NUMBERS ONR #N00014-93-1-0827		
6. AUTHOR(S) Jerome T. Chu, Student Sheng S. Li, Professor				
7. PERFORMING ORGANIZATION NAME(S) AND ADDRESS(ES)  University of Florida Gainesville, FL 32611-6200		8. PERFORMING ORGANIZATION REPORT NUMBER  92120712		
9. SPONSORING/MONITORING AGENCY NAME(S) AND ADDRESS(ES) US Navy, Office of Naval Research 800 North Quincy Street, Code 1512B:SM Arlington, VA 22217-5000		10. SPONSORING/MONITORING AGENCY REPORT NUMBER		
11. SUPPLEMENTARY NOTES				
12a. DISTRIBUTION / AVAILABILITY STATEMENT  Approved for public release, distribution unlimited.		12b. DISTRIBUTION CODE		
13. ABSTRACT (Maximum 200 words) During this reporting period, we have made excellent progress towards the program goals. A new compressively strained p-type quantum well infrared photodetector (QWIP) was developed using the step-bound-to-miniband intersubband transition. The observed response peak was at 10.4 $\mu\text{m}$ . At a temperature of $T = 65\text{ K}$ , the maximum responsivity at $V_b = 3.0\text{ V}$ was found to be 28 mA/W. This device is BLIP limited when $T \leq 40\text{ K}$ with the corresponding bias at $ V  \leq 2\text{ V}$ . The calculated spectral detectivity at the $T = 65\text{ K}$ and $V = 1\text{ V}$ operating point was $D^* = 1.4 \times 10^9\text{ cm Hz}^{1/2}/\text{W}$ . We also characterized the dark current noise performance of two p-type QWIPs with spectral response peaks at 7.4 and 9.2 $\mu\text{m}$ . Using a newly developed model for the dark current, we were able to accurately model the dark current of these devices at low applied biases.				
14. SUBJECT TERMS  P-type strained layer InGaAs/GaAs quantum well infrared photodetectors (QWIPs), intersubband absorption, dark current, responsivity, detectivity.		15. NUMBER OF PAGES		
		16. PRICE CODE		
17. SECURITY CLASSIFICATION OF REPORT Unclassified	18. SECURITY CLASSIFICATION OF THIS PAGE	19. SECURITY CLASSIFICATION OF ABSTRACT	20. LIMITATION OF ABSTRACT  Unlimited	

**Fifth Semi-Annual Progress Report (7/26/95-2/15/96)**

**Project Title: The Development of Normal Incidence High Performance  
P-type Strained Layer InGaAs/AlGaAs Quantum Well  
Infrared Photodetectors**

**Program Manager:** Max N. Yoder, Office of Naval Research, Code 3140, Arlington, VA.

**Principal Investigator:** Sheng S. Li, Professor, University of Florida, Gainesville, FL.

**Student :** Jerome T. Chu

**Project Objective:**

The objective of this project is to perform theoretical and experimental studies of dark current, photocurrent, optical absorption, spectral responsivity, noise, and detectivity for the normal incidence strained layer p-type III-V semiconductor quantum well infrared photodetectors (QWIPs) developed under this program. The material systems under investigation include InGaAs/InAlAs on InP substrates and GaAs/InGaAs or AlGaAs/InGaAs on GaAs substrates. The project will study the usage and effects of biaxial tension and compressional strain on the material systems and their effects towards photodetector design.

## I. Introduction

During the period of July 26, 1995 to February 15, 1996, significant progress has been made towards the design, fabrication, and characterization of new strained layer p-type GaAs/InGaAs on GaAs and InGaAs/AlGaAs on GaAs quantum-well infrared photodetectors (P-QWIPs) in the 8-14  $\mu\text{m}$  range for staring focal plane arrays (FPAs). Specific tasks performed during this period include: (i) the design, fabrication, and characterization of the first p-type QWIP to utilize the step bound-to-miniband transition scheme with a peak detective wavelength at 10.4  $\mu\text{m}$  and (ii) the modeling and characterization of the dark current of p-type QWIPs at low applied biases. The following sections of this report will cover the technical results of the study obtained during this reporting period and the research accomplishments and publications. A summary of the various types of p-QWIPs studied is listed at the end of this report in table 1.

## II. Technical Results

### 2.1 Research Accomplishments and Publications

1. The design, growth, fabrication, and characterization of a Be-doped compressively strained InGaAs/GaAs/AlGaAs p-QWIP on SI GaAs with a peak detection wavelength at 10.4  $\mu\text{m}$ , which utilizes the step bound-to-miniband transition scheme for photoexcited carrier transport. The observed peak responsivity at  $T=65\text{ K}$  and  $V_b=3.0\text{ V}$  was 28 mA/W. This device was BLIP limited when  $T \leq 40\text{ K}$  with the corresponding bias of  $\leq |2V|$ . The calculated spectral detectivity at  $T=65\text{ K}$  and  $V=1.0\text{ V}$  was determined to be  $1.4 \times 10^9\text{ cm}\sqrt{\text{Hz}}/\text{W}$ .
2. The characterization of the dark current noise performance of a 7.4  $\mu\text{m}$  peak p-type compressively strained-layer quantum well infrared photodetector between  $10^1$  and  $10^5\text{ Hz}$ . A value of  $2.6 \times 10^{-13}\text{ cm}^2$  was determined for the scattering cross section at 100 K.
3. The noise characterization of a p-type compressively strained QWIP with a detection peak at 9.2  $\mu\text{m}$  at low applied biases. Using this data, we were able to model the

dark current characteristics of the p-type QWIPs. Excellent agreement was obtained between the measured and calculated dark I-V characteristics.

#### **A. Journal Papers:**

1. Y. H. Wang, S. S. Li, and J. Chu and Pin Ho, "An Ultra-low Dark Current P-type Strained-layer InGaAs/InAlAs Quantum Well Infrared Photodetector with Background Limited Performance (BLIP)" *Appl. Phys. Letts*, **64**(4), 727 (1994).
2. Y. H. Wang, S. S. Li, and J. Chu and Pin Ho, "A Normal Incidence P-type Compressive Strained-Layer InGaAs/GaAs Quantum Well Infrared Photodetector for Mid-Wavelength Infrared (MWIR) and Long-Wavelength Infrared (LWIR) Detection" *J. Appl. Phys.*, **76**(10), 6009 (1994).
3. D. C. Wang, G. Bosman, and S. S. Li, "Noise Characterization and Device Parameter Extraction on a p-type Strained Layer Quantum Well Infrared Photodetector", to be published in *J. Appl. Phys.*, February 1996.
4. J. Chu, S. S. Li, and P. Ho, "A New Compressively Strained P-type Quantum Well Infrared Photodetector Using the Step Bound-to-miniband Detection Scheme", to be submitted to *Appl. Phys. Lett.*, 1996.
5. J. Chu, S. S. Li, and P. Ho, "A Study of Compressively Strained P-type Quantum Well Infrared Photodetectors", to be submitted to *J. Appl. Phys.*, 1996.
6. D. C. Wang, G. Bosman, and S. S. Li, "Current Conduction and Noise Characteristics of Quantum Well Infrared Photodetectors Under Low Bias Operation", *Appl. Phys. Lett.*, accepted for publication, 1996.

#### **B. Conference Presentations:**

1. S. S. Li, J. Chu, and Y. H. Wang, "A Normal Incidence P-type Strained Layer InGaAs/InAlAs Quantum Well Infrared Photodetector with Background Limited Performance at 77 K", presented at the 1994 SPIE symposium, Orlando, FL, April 4-8, 1994. Full paper published in the conference proceedings.

2. Pin Ho, Y. H. Wang, S. S. Li, and J. Chu, "MBE Growth of P-type Strained-layer InGaAs/InAlAs QWIPs", presented at the 1994 14th North American Conference on Molecular-beam Epitaxy, Urbana-Champaign, IL, October 10-12, 1994.
3. Y. H. Wang, J. Chu, S. S. Li, and Pin Ho, "A Normal Incidence P-type Compressive Strained-Layer InGaAs/GaAs Quantum Well Infrared Photodetector", 2nd. International Conference on 2-20  $\mu\text{m}$  Wavelength Infrared Detectors and Arrays, Miami Beach, FL, October 9-14, 1994. Full paper published in the conference proceedings.
4. S. S. Li, Y. H. Wang, and J. Chu, "A New Class of Normal Incidence Strained-Layer III-V Quantum Well Infrared Photodetectors", presented at the 1994 LEOS Conference, Boston, MA, October 31-November 3, 1994. Full paper published in the conference proceedings.
5. J. Chu, Y. H. Wang, S. S. Li, and Pin Ho, "A New Compressively Strained InGaAs/AlGaAs p-type Quantum Well Infrared Photodetector with Ultra-low Dark Current and Detective Peaks in the LWIR and MWIR Bands", presented at the 3rd. International Symposium on Long Wavelength Infrared Detectors and Arrays: Physics and Applications, Chicago, IL, October 9-11, 1995. Full paper published in the conference proceedings.
6. J. Chu, S. S. Li, S. Y. Yen, A. Chin, and K. M. Chang, "Investigation of Si-doped p-type GaAs/AlGaAs and Strained-layer InGaAs/AlGaAs Quantum Well Infrared Photodetectors grown on (311) GaAs for Mid- and Long-Wavelength IR Detection", presented at the 3rd. International Symposium on Long Wavelength Infrared Detectors and Arrays: Physics and Applications, Chicago, IL, October 9-11, 1995.
7. D. Wang, G. Bosman, S. S. Li, and J. Chu, "Noise Performance of p-type Strained Layer Quantum Well Infrared Photodetectors", presented at the 3rd. International Symposium on Long Wavelength Infrared Detectors and Arrays: Physics and Applications, Chicago, IL, October 9-11, 1995. Full paper published in conference proceedings.
8. S. S. Li, J. Chu, and Y. H. Wang, "P-type Strained-layer III-V Quantum Well Infrared Photodetectors for Long-wavelength Infrared Focal Plane Array Applications", invited paper, presented at the Int. Conf. on Intersubband Transitions in Quantum Wells

(ITQW '95), Kibbutz Ginosar, Isreal, Oct. 23-26, 1995. Full paper published in the conference proceedings.

## 2.2 P-QWIP Operation and Design Theory

With the advent of molecular beam epitaxial technologies in the last few decades, device structures utilizing heterostructure quantum wells have been heavily explored. N-type quantum well infrared photodetectors (QWIPs) have been extensively studied in recent years<sup>1-2,28</sup>. These systems use GaAs/AlGaAs and InGaAs/InAlAs structures for detection in the 3 - 5  $\mu\text{m}$  mid-wavelength infrared (MWIR) and 8 - 14  $\mu\text{m}$  LWIR atmospheric transmission windows. Since n-type GaAs/InGaAs and InGaAs/InAlAs QWIPs have inherently low electron effective masses and high electron mobilities, they offer excellent infrared (IR) detection properties. Due to the quantum mechanical selection rules which prohibit normal incidence intersubband absorption, focal plane arrays (FPA) using n-type QWIPs must use either metal or dielectric gratings to couple normal incidence IR radiation into the quantum well<sup>2-4</sup>. In contrast, because of the mixing between the light hole and heavy hole states under either biaxial tension or compressive strain, normal incidence illumination is allowed for the intersubband transition in p-type QWIPs; thus eliminating the need for metal or dielectric grating couplers.

### 2.2.1 P-QWIP Physics

#### 2.2.1.1 Strained Layer Growth Limitations and Theory

P-type QWIPs using valence intersubband transitions have been demonstrated<sup>5-7</sup> in lattice-matched GaAs/AlGaAs and InGaAs/InAlAs material systems. In general, intersubband transitions excited by normal incidence radiation in p-type quantum wells are allowed since a linear combination of p-like valence band Bloch states exists, which provides a nonzero coupling between the normal radiation field and valence band Bloch states. The strong mixing between the heavy hole and the light hole states greatly enhances intersubband absorption. The drawback of using lattice-matched systems is the fact that the intersubband transition occurs between the heavy hole ground states and the upper excited states. Because of the relatively large heavy hole effective mass when compared to the electron effective

mass, relatively weak absorption and therefore similarly low responsivity is predicted in the IR wavelength range when compared to n-type QWIPs. In order to increase the absorption characteristics and responsivity of P-QWIPs, biaxial stress is introduced into the well layers of the QWIP structure. If the intentionally introduced biaxial stress between the well layers and the barrier layers contained in the layer thickness (the total thickness of the wells and barriers) in the P-QWIP structure is less than the critical thickness, then pseudomorphic or coherent heterointerfaces can be grown without the introduction of defects between the layers. Based upon the force balance model<sup>8,29-30</sup>, the equilibrium critical layer thickness,  $L_c$ , for an epilayer with the lattice constant,  $a$ , grown on a substrate with a lattice constant,  $a_s$ , is given as

$$L_c = \left( \frac{a}{\sqrt{2}\delta_o} \right) \frac{1 - \nu \cos^2 \Theta}{8\pi(1 + \nu) \cos \alpha} \left[ 1 + \ln(h\sqrt{2}/a) \right], \quad (1)$$

where  $h$  is the epilayer thickness,  $\Theta$  is the angle between the dislocation line and the Burges' vector,  $\alpha$  is the angle between the slip direction and the layer plane direction,  $\delta_o$  is the lattice-mismatch or the in-plane strain, and  $\nu$  is the Poisson ratio.  $\delta_o$  is defined as  $\delta_o = (a_s - a)/a$  where  $\delta_o > 0$  for tensile strain and  $\delta_o < 0$  for compressive strain. Similarly,  $\nu$  is defined as  $\nu = -C_{12}/C_{11}$ .  $C_{ij}$ 's are the elastic constants and can be found in reference 9.

The strained-layers have the same effective in-plane lattice constant,  $a_{||}$  (i.e.,  $a_{x,y}$ ), and can store the excess energy due to the elastic strain within the layers. The in-plane lattice constant,  $a_{||}$ , can be expressed by<sup>8</sup>

$$a_{||} = a_1 \left[ 1 + \delta_o / \left( 1 + \frac{\xi_1 L_1}{\xi_2 L_2} \right) \right], \quad (2)$$

where  $a_{1,2}$  and  $L_{1,2}$  are the individual layer lattice constants and thicknesses, respectively, and  $\xi_{1,2}$  are the shear moduli as described by  $\xi = (C_{11} + C_{12} - 2C_{12}^2/C_{11})$ , where the  $C_{ij}$ 's are elastic constants for the strained material.  $\delta_o$  denotes the lattice mismatch between layers and  $a_{1,2}$  are the lattice constants of the strained well and the substrate (or barrier) respectively. When  $a_{||} \neq a_s$ , the coherently strained superlattice structure is no longer in equilibrium with the substrate. If the lattice constant of the barrier layers is equal to that of the substrate, the strain will be completely accommodated in the well layers with no strain in the barrier layers. However, Hull et al.<sup>22</sup> showed that if the individual layer thickness in the superlattice is less than its critical thickness, even though  $a_{||} \neq a_s$ , the loss of coherence only occurs at the interface between the whole superlattice and the substrate, while the



superlattice itself remains coherent.

### 2.2.1.2 Strain Induced Energy Band Shifts

If the QWIP structure is grown along the [100] direction and the strained-layer is within the critical thickness,  $L_c$ , then a pseudomorphic or coherent heterointerface can be obtained and the components of the strain tensor  $[e]$  are simplified to the expressions given by

$$e_{xx} = e_{yy} = e_{||} \quad (3)$$

$$e_{zz} = -e_{||} \left( \frac{2C_{12}}{C_{11}} \right) \quad (4)$$

$$e_{xy} = e_{yz} = e_{zx} = 0. \quad (5)$$

In addition to altering the physical parameters of the QWIP, lattice strain can also induce energy band shifts, which can be used to alter the absorption characteristics of the QWIP. The strain induced energy band shifts for the conduction band, the heavy hole subband, and light hole subband can be approximated as follows.

$$\Delta E_c = 2c_1 \frac{C_{11} - C_{12}}{C_{11}} \delta_o \quad (6)$$

$$\Delta E_{hh} = b \frac{C_{11} + C_{12}}{C_{11}} \delta_o \quad (7)$$

$$\Delta E_{lh} = -\Delta E_{hh} + \frac{(\Delta E_{hh})^2}{2\Delta_o} \quad (8)$$

where  $c_1$  is the combined hydrostatic deformation potential which characterizes the splitting of the  $\Gamma_8$  valence band under strain, and  $b$  is the shear deformation potential, and  $\Delta_o$  is the spin orbit split-off energy<sup>9</sup>. The total hydrostatic deformation potential ( $c_1 + V_v$ ), where  $V_v$  is the valence band deformation potential, can be expressed by<sup>10</sup>

$$c_1 + V_v = -\frac{1}{3}(C_{11} + 2C_{12}) \frac{dE_g^o}{dP}, \quad (9)$$

where  $dE_g^o/dP$  is the unstrained energy bandgap change with respect to the unit pressure.

The effect of strain on the energy band structure results in the splitting of the heavy hole and light hole band at the valence band zone center<sup>11</sup> (i.e., the in-plane wavevector  $k_{||} = 0$ ), which is degenerate in the unstrained case. When tensile strain is applied between the quantum well and the barrier layers<sup>12-14</sup> along the superlattice growth  $z$ -direction, the strain can push the light hole levels upwards and pull the heavy hole levels downwards. We

can therefore expect that heavy hole and light hole states are inverted at specific lattice strains and quantum well thicknesses. This phenomena will in turn cause the intersubband transitions in a QWIP structure to take place from the populated light hole ground state to the upper energy band states. Since the light hole has a small effective mass (comparable to the electron effective mass), the optical absorption and spectral responsivity in p-type QWIPs can be greatly enhanced, as a result of introducing strain in the quantum well. In addition to the utilization of the light hole states for their small effective masses, etc., certain heavy hole states under compressional strain may also have similar characteristics, like high mobilities, small effective masses, and long mean free paths; which in turn favorably alter the intersubband absorption and transport characteristics, as shown by Hirose, et al.<sup>31</sup>. This is achieved by distorting the heavy hole valence band at and near the zone center via the introduction of compressional strain.

### 2.2.1.3 Energy Band Calculations

To calculate the locations of the energy subbands, we can use the transfer matrix method (TMM)<sup>13,15</sup>, based on the eight-band  $\mathbf{k} \cdot \mathbf{p}$  model. This model is represented by the Luttinger-Kohn Hamiltonian<sup>16-17</sup>,  $H_t$ , which describes the unstrained semiconductor.

$$H_t = H + V(z) \quad (10)$$

where

$$H = \begin{bmatrix} H_{11} & H_{12} & H_{13} & H_{14} \\ H_{21} & H_{22} & H_{23} & H_{24} \\ H_{31} & H_{32} & H_{33} & H_{34} \\ H_{41} & H_{42} & H_{43} & H_{44} \end{bmatrix} \quad (11)$$

with:

$$\begin{aligned} H_{11} &= \frac{\gamma_1 + \gamma_2}{2}(k_x^2 + k_y^2) + \frac{\gamma_1 - \gamma_2}{2}k_z^2 \\ H_{22} &= \frac{\gamma_1 - \gamma_2}{2}(k_x^2 + k_y^2) + \frac{\gamma_1 + \gamma_2}{2}k_z^2 \\ H_{12} &= i\sqrt{3}\gamma_3(k_x - ik_y)k_z \\ H_{13} &= \frac{\gamma_2\sqrt{3}}{2}(k_x^2 - k_y^2) - i\sqrt{3}\gamma_3k_xk_y \\ H_{21} &= H_{12}^*, & H_{13} &= H_{31}^*, & H_{24} &= H_{13} \\ H_{34} &= H_{12}^*, & H_{42}^* &= H_{13}^*, & H_{43} &= H_{12}^* \end{aligned}$$

$$H_{14} = H_{23} = H_{32} = H_{41} = 0$$

and  $V(z)$  is a step function where  $V(z)$  vanishes inside the well layers and equals  $V_o$  in the barrier layers. The effect of strain is included by adding the Pikus-Bir Hamiltonian<sup>18</sup>,  $H_s$ , to the general Luttinger-Kohn Hamiltonian. As shown below, the strain Hamiltonian for the well material is a diagonal matrix.

$$H_s = \begin{bmatrix} -\Delta E_c - \Delta E_{hh} & 0 & 0 & 0 \\ 0 & -\Delta E_c + \Delta E_{hh} & 0 & 0 \\ 0 & 0 & -\Delta E_c + \Delta E_{hh} & 0 \\ 0 & 0 & 0 & \Delta E_c + \Delta E_{hh} \end{bmatrix} \quad (12)$$

Using the aforementioned techniques, we can numerically calculate the energy of the zone-center valence subband levels as a function of well width for any material system under tensile or compressional strain and also determine the change in the valence subband structures.

All of the previously described calculations are derived from the multiband effective mass  $\mathbf{k} \cdot \mathbf{p}$  model for a coherently strained structure, which is based upon the perturbation approximation. In the  $\mathbf{k} \cdot \mathbf{p}$  model, the interactions of S-P type coupling among conduction (C), light-hole (LH), heavy-hole (HH), and spin-orbit (SO) states combined with spin-orbit like coupling are taken into consideration to derive the band structures. This results in an  $8 \times 8$   $\mathbf{k} \cdot \mathbf{p}$  Hamiltonian and momentum matrix elements. Using the perturbation approximation, a set of wave functions of  $S_{1/2}$ :  $|1/2, \pm 1/2\rangle_c$ ;  $P_{3/2}$ :  $|3/2, \pm 3/2\rangle$ ,  $|3/2, \pm 1/2\rangle$ ; and  $P_{1/2}$ :  $|1/2, \pm 1/2\rangle$  are used to represent the unperturbed and unstrained basis in the  $|J, m_j\rangle$  presentation<sup>23</sup>.  $m_j = \pm 1/2$  represents either the electron or LH states, while  $m_j = \pm 3/2$  denotes the HH or heavy particle states. A slightly simplified  $6 \times 6$   $\mathbf{k} \cdot \mathbf{p}$  Hamiltonian can be used to roughly predict the P-like properties of the coherently strained layers by considering the S-like conduction band states as a perturbation, if a large enough bandgap exists, like in InGaAs and GaAs layers. The wave functions of the coherently strained superlattice at the zone center ( $\mathbf{k}=0$ ) are given by<sup>24</sup>

$$|3/2, \pm 3/2\rangle \quad HHstates \quad (13)$$

$$\gamma|3/2, \pm 1/2\rangle + \beta|1/2, \pm 1/2\rangle \quad LHstates \quad (14)$$

$$-\beta|3/2, \pm 1/2\rangle + \gamma|1/2, \pm 1/2\rangle \quad SOstates \quad (15)$$

where  $\gamma$  and  $\beta$  are constants which are dependent on the strain parameters. Note that the heavy-hole states,  $|3/2, \pm 3/2\rangle$ , are still decoupled from the other valence band states even under biaxial stress at the zone center, while the light-hole and spin-orbit split off states are coupled at  $\mathbf{k}=0$ . However, the HH, LH, and SO states are mixed<sup>25,26</sup> in the coherently strained superlattice at off zone center ( $\mathbf{k}\neq 0$ ). This mixing between the states with different  $m_j$ 's is due to the boundary conditions across the interface of the quantum well layers. By examining the  $\mathbf{k} \cdot \mathbf{p}$  matrix, we can see that the interaction between the different  $m_j$  states is proportional to the transverse components of the wave vector,  $k_{x,y}$ , so that the HH states are decoupled when  $k_{x,y}=0$ . It is interesting to note that the  $k_{x,y}$ 's are conserved across the interfaces since the interface potential depends only on  $z$ , the quantum well growth direction. Thus the band mixing can be significant if the  $\Gamma$ -bandgap is small, e.g., with GaAs and InGaAs, and if the LH and SO bands involved in the transition have a large  $k_z$  value<sup>25</sup>.

Since the heavy hole and light hole valence subbands are non-degenerate following the introduction of strain into the QWIP structure, a simpler method can be used to determine the energies of the subbands. By using the parabolic band approximation near the valence band zone-center, and the energy band shifts for the conduction band minimum, heavy hole subband maximum, and light hole subband maximum, we can utilize the simpler two-band Hamiltonian for electrons just by finding the effective mass of the carriers (i.e., heavy-hole effective mass and light-hole effective mass) and the barrier heights for each carrier type. Although this does not simultaneously determine the energy levels of both carriers, it does allow accurate predictions of the energy subbands. When compared to the direct calculation of the energy subbands, the two-band approximation yields accurate results when compared to the direct calculation results<sup>13,18</sup>. One limitation of the TMM is that this method cannot calculate the energy levels of the allowed energy subbands in the continuum states. In order to determine the transition energy from the ground state to the continuous state, we used the Kronig-Penney model to determine the locations of the allowed energy bands in the continuum states.

When a biaxial internal tension is applied to the well material, the strain pulls the LH subbands up with respect to the HH subbands for a given well thickness. While quantum confinement effects tend to push the LH subbands down with respect to the HH subbands.

As the well width is increased above a certain value, the strain effect can overcome the quantum confinement effect and therefore induce the inversion of the heavy hole and light hole subbands at the ground state. In contrast, with the application of compressional strain on the well layers, the strain forces the LH subbands down with respect to the HH subbands for a given well thickness.

#### 2.2.1.4 The Transfer Matrix Method for the Calculation of Transmission Probability

The transfer matrix method (TMM) <sup>33</sup> allows the calculation of the transmission probability through a superlattice. Like any typical quantum mechanical barrier or well, the carrier conduction in each layer of the superlattice consists of the superposition of two components propagating forwards and backwards. The complete wave function can be expressed as

$$\psi_i = \psi_i^+ e^{+ik_i} e^{-\Delta_i} + \psi_i^- e^{-k_i} e^{+\Delta_i} \quad (16)$$

where

$$\begin{aligned} \Delta_1 &= \Delta_2 = 0 \\ \Delta_i &= k_i(d_2 + d_3 + \dots + d_i) \\ i &= 3, 4, \dots, N \\ k_i &= \left[ \frac{2m_i^*}{\hbar^2} (E - E_i) \right]^{1/2}, \end{aligned}$$

where  $\psi_i^+$  and  $\psi_i^-$  represent the magnitudes of the wave functions propagating in the forward, or  $+z$  direction and the backwards, or  $-z$  direction, respectively. While  $N$  is the number of periods in the superlattice,  $d_i$  is the thickness of the  $i$ -th layer in the superlattice,  $m_i^*$  is the effective mass of the particle in the  $i$ -th superlattice layer, and  $E_i$  is the potential energy of the  $i$ -th layer. Since the wave function,  $\psi$ , and its derivative,  $d\psi/dz$ , are continuous at the boundaries, the wave functions then become

$$\psi_i^+ = (e^{-i\delta_i} \psi_{i+1}^+ + r_i e^{-i\delta_i} \psi_{i+1}^-) / t_i \quad (17)$$

$$\psi_i^- = (r_i e^{i\delta_i} \psi_{i+1}^+ + e^{i\delta_i} \psi_{i+1}^-) / t_i. \quad (18)$$

The recurrence relationship of the wave functions can be written in matrix form as

$$\begin{pmatrix} \psi_i^+ \\ \psi_i^- \end{pmatrix} = \frac{1}{t_i} \begin{pmatrix} e^{-i\delta_i} & r_i e^{-i\delta_i} \\ r_i e^{i\delta_i} & e^{i\delta_i} \end{pmatrix} \begin{pmatrix} \psi_{i+1}^+ \\ \psi_{i+1}^- \end{pmatrix}, \quad (19)$$

where at normal incidence

$$r_i = \frac{k_i - k_{i+1}}{k_i + k_{i+1}}, \quad (20)$$

$$t_i = \frac{2k_i}{k_i + k_{i+1}}, \quad (21)$$

and

$$\delta_i = k_i d_i. \quad (22)$$

Which gives us the following form for determining the  $N + 1$ -th wave functions

$$\begin{pmatrix} \psi_1^+ \\ \psi_1^- \end{pmatrix} = S_1 \begin{pmatrix} \psi_2^+ \\ \psi_2^- \end{pmatrix} = S_1 S_2 \begin{pmatrix} \psi_3^+ \\ \psi_3^- \end{pmatrix} = S_1 S_2 \cdots S_N \begin{pmatrix} \psi_{N+1}^+ \\ \psi_{N+1}^- \end{pmatrix}, \quad (23)$$

where

$$S_i = \frac{1}{t_i} \begin{pmatrix} e^{-i\delta_i} & r_i e^{-\delta_i} \\ r_i e^{i\delta_i} & e^{i\delta_i} \end{pmatrix}. \quad (24)$$

Since there is no backwards, or in the  $-z$  direction, propagation in the  $N + 1$ -th layer, the magnitude of the wave function  $\psi_{N+1}^- = 0$ . Thus we can find the  $\psi_i^+$  term of  $E_1^+$ , in the  $i$ -th layer ( $i = 2, 3, 4, \dots, N + 1$ ).

If we determine the quantity,  $\psi_i^+/\psi_1^+$ , as a function of  $E_1$ , then we will know the locations of the resonant peaks. The transmission probability can be expressed as

$$|T \cdot T| = \left| \frac{\psi_i^+}{\psi_1^+} \right|^2. \quad (25)$$

#### 2.2.1.5 Determination of Intersubband Transitions and Absorption Coefficients

In addition to the energy level and energy band locations, the calculation of intersubband and interband transitions are also of great interest. In order to determine the intersubband and interband transitions in a p-type strained layer QWIP, the usage of the  $6 \times 6$  Hamiltonian which includes the previously mentioned  $\mathbf{k} \cdot \mathbf{p}$  Hamiltonian<sup>16-17,24</sup> and the strain Hamiltonian<sup>18</sup>. Since the strain and the spin-orbit coupling terms do not lift the spin degeneracy, the  $6 \times 6$  Hamiltonian matrix can then be factorized into two  $3 \times 3$  irreducible matrices. The assumption that the Fermi distribution function is equal to one for the confined ground state and equal to zero for the excited states in equilibrium is used to simplify

the calculation without loss of accuracy. The absorption coefficient for the intersubband or interband transition between the initial ground state,  $i$ , and the final continuum state,  $f$ , is given by<sup>27</sup>

$$\alpha_i(\omega) = \sum_f \frac{4\pi^2 e^2}{n_r c m_o^2 \omega} \int_{BZ} \frac{2d\mathbf{k}}{(2\pi)^3} \left[ (f_i - f_f) |\hat{\mathbf{e}} \cdot \mathbf{P}_{i,f}|^2 \frac{\Gamma/2\pi}{[\Delta_{i,f}(\mathbf{k}) - \hbar\omega]^2 + (\Gamma^2/4)} \right] \quad (26)$$

where  $n_r$  is the refractive index in the quantum well,  $m_o$  is the free electron mass,  $\Delta_{i,f}$  is the energy difference between the initial ground state,  $i$ , of energy  $E_i(\mathbf{k})$  and the final state,  $f$ , with the corresponding energy of  $E_f(\mathbf{k})$ .  $\hat{\mathbf{e}}$  and  $\omega$  are the unit polarization vector and the frequency of the incident IR radiation, respectively,  $f_i$  and  $f_f$  are the Fermi distribution functions of the initial and final states, and  $\Gamma$  is the full width of level broadening.  $\Gamma \sim \hbar/\tau_{if}$ , where  $\tau_{if}$  is the lifetime between the initial,  $i$ , and final,  $f$ , states.  $|\hat{\mathbf{e}} \cdot \mathbf{P}_{i,f}|$  are the optical transition elements between the quantum well valence subband ground states,  $i$ , and the continuum subband states,  $f$ , in the HH, LH, and SO bands; which can be derived from the two  $3 \times 3$   $\mathbf{k} \cdot \mathbf{p}$  matrix elements as shown below.

Using the following  $3 \times 3$  optical matrix,

$$\frac{m_o}{\hbar} \begin{bmatrix} T_{HH} & T_{HL} & T_{HS} \\ T_{LH} & T_{LL} & T_{LS} \\ T_{SH} & T_{SL} & T_{SS} \end{bmatrix}, \quad (27)$$

the optical matrix elements,  $|\hat{\mathbf{e}} \cdot \mathbf{P}_{i,f}|$ , can be obtained. These matrix elements have the same form as the  $\mathbf{k} \cdot \mathbf{p}$  matrix elements except that the  $k_i k_j$ 's are replaced with  $k_i \epsilon_j + k_j \epsilon_i$  multiplied by a constant factor of  $m_o/\hbar$ .<sup>27</sup> The  $T_{ij}$ 's are defined as follows:

$$T_{HH} = 2(A - B)\epsilon_z k_z + (2A + B)(\epsilon_x k_x + \epsilon_y k_y), \quad (28)$$

$$T_{LL} = 2(A + B)\epsilon_z k_z + (2A - B)(\epsilon_x k_x + \epsilon_y k_y), \quad (29)$$

$$T_{SS} = 2A(\epsilon_x k_x + \epsilon_y k_y + \epsilon_z k_z) \quad (30)$$

$$\begin{aligned} T_{HL} = & i \frac{1}{\sqrt{3}} N (\epsilon_x \cos \eta - \epsilon_y \sin \eta) k_z - i \frac{1}{3} N \epsilon_z k_{\parallel} \\ & - \sqrt{3} B (\epsilon_x k_x - \epsilon_y k_y) \cos \chi \\ & + \frac{1}{\sqrt{3}} N (\epsilon_x k_y + \epsilon_y k_x) \sin \chi, \end{aligned} \quad (31)$$

$$T_{HS} = \frac{1}{\sqrt{6}} N (\epsilon_x \cos \eta + \epsilon_y \sin \eta) k_z + \frac{1}{6} N \epsilon_z k_{\parallel}$$

$$\begin{aligned}
& +i\sqrt{6}B(\epsilon_x k_x - \epsilon_y k_y) \cos \chi \\
& -\frac{2}{\sqrt{6}}N(\epsilon_x k_y + \epsilon_y k_x) \sin \chi,
\end{aligned} \tag{32}$$

$$\begin{aligned}
T_{LS} = & \left[ i2\sqrt{2}B\epsilon_z + \frac{1}{\sqrt{2}}N\epsilon_x \cos(\chi - \eta) - \epsilon_y \sin(\chi - \eta) \right] k_z \\
& -i\sqrt{2}B(\epsilon_x k_x + \epsilon_y k_y) \\
& -\frac{1}{\sqrt{2}}N\epsilon_z k_{\parallel} \cos(\chi - 2\eta),
\end{aligned} \tag{33}$$

$$T_{SH} = T_{HS}^*, \tag{34}$$

$$T_{SL} = T_{LS}^*, \tag{35}$$

$$T_{LH}^* = T_{HL}^*. \tag{36}$$

Here  $A, B, N, \chi, \eta$  are inverse mass band parameters.<sup>27</sup>

#### 2.2.1.6 Photoconductive Detection Mode Operation

When IR radiation impinges on a photoconductor, the photoconductive material undergoes a physical change characterized by a change in resistance,  $\Delta R_d$ . This change in resistance is due to the photo-excitation of carriers, forming mobile excess carriers in the photoconductor. The excess photogenerated carriers,  $\Delta n$ , can be expressed as

$$\Delta n = \frac{\eta \Delta \Phi \tau_L}{V_d} \tag{37}$$

where,  $\eta$ , is the quantum efficiency,  $\Delta \Phi$  is the incident photon flux,  $\tau_L$  is the excess carrier lifetime, and  $V_d$  is the volume of the detector. These photogenerated carriers are transported out of the detector under the influence of the applied external bias, which results in a photovoltage signal. The change in the output photovoltage,  $\Delta V_o$ , due to the resistance change is given by

$$\Delta V_o = -\frac{V_a R_L \Delta R_d}{(R_L + R_d)^2}, \tag{38}$$

where  $R_L$  is the load resistance and its value is typically chosen to be about equal to  $R_d$ , the detector resistance, to match loads and to optimize the output signal.

#### 2.2.2 P-QWIP Figures of Merit

Although our band structure and absorption calculations can be used to determine the positions of the subbands in the quantum wells, and hence determine the peak absorption



wavelength of the QWIP, many other factors must be taken into account to design a QWIP with the correct detection peak. Generally, for a high-performance QWIP, the responsivity must be high, while the noise current, and hence the dark current, must be low.

### 2.2.2.1 Spectral Responsivity

The responsivity,  $R$ , for a photodetector may be expressed as<sup>19</sup>

$$R = \frac{q\lambda\eta}{hc} G = \frac{q}{h\nu} \eta_c, \quad (39)$$

where  $q$  is the electronic charge,  $\lambda$  is the wavelength of the incident photon,  $h$  is the Planck constant,  $c$  is the speed of light,  $\eta$  is the quantum efficiency,  $\eta_c$  is the collection efficiency,  $\nu$  is the incident frequency, and the photoconductive gain is  $G$ . The quantum efficiency and photoconductive gain are described, respectively, by<sup>19</sup>

$$\eta = A(1 - R)[1 - \exp(-B\alpha l_{qw})] \quad (40)$$

$$G = \frac{L}{t_c} \quad (41)$$

where  $A$  is a constant that is polarization dependent,  $\alpha$  is the absorption coefficient of the quantum well,  $l_{qw}$  is the total width of all quantum well regions,  $L$  is the mean free path of the carrier,  $R$  is the reflection coefficient, and  $t_c$  is the total width of all quantum well and barrier regions.  $B$  is a constant dependent on the number of passes IR radiation makes through the photodetector. For n-type QWIPs,  $A=0.5$ , while for p-type QWIPs  $A=1$ . The mean free path of the carrier may be expressed as<sup>19</sup>

$$L = \tau T_{qw} \mu_{eff} \mathcal{E}, \quad (42)$$

where  $\tau$  is the well recapture lifetime of the carrier,  $T_{qw}$  is the transmission coefficient over the quantum well,  $\mu_{eff}$  is the effective mobility of the carrier, and  $\mathcal{E}$  is the electric field. The effective mobility for a two-band transport model is shown to be<sup>19</sup>

$$\mu_{eff} = \frac{\Delta p_{lh} \mu_{lh} + \Delta p_{hh} \mu_{hh}}{\Delta p_{lh} + \Delta p_{hh}}, \quad (43)$$

where  $\Delta p_{hh}$  and  $\Delta p_{lh}$  are the concentrations of optically induced heavy- and light- hole carriers, respectively, and  $\mu_{hh}$  and  $\mu_{lh}$  are the respective heavy and light hole mobilities. When only the ground state is completely occupied, either  $\Delta p_{lh}$  or  $\Delta p_{hh}$ , the optically

induced light holes or the optically induced heavy holes dominate, so that we may estimate  $\mu_{eff}$  as the in-plane effective mass of the ground state carriers.

#### 2.2.2.2 QWIP Collection Efficiency

A figure of merit that can be easily quantified by simple measurements is the collection efficiency,  $\eta_c$ . The collection efficiency describes the ease in which the energy from the incident photon flux is converted into mobile carriers which are swept out of the QWIP by the applied bias and collected; and is defined as the product of the quantum efficiency,  $\eta$ , and the photoconductive gain,  $G$ .

$$\eta_c = \eta G \quad (44)$$

In addition to being expressed as the mean free path over the total width of the quantum wells and barriers,  $G$  can be viewed as the ratio of the carrier transport lifetime,  $\tau_L$ , to the transit time,  $\tau_T$ , through the QWIP. Empirically, the photoconductive gain can be described in terms of the capture or trapping probability,  $p_c$ ,<sup>34-36</sup>

$$G = \frac{1}{N p_c (1 + p_c)}, \quad (45)$$

and  $N$  is the number of wells. If  $p_c$  is small, then  $G$  can be approximated as,  $G \simeq 1/N p_c$ .

Physically, the trapping probability is defined as the ratio of the escape time from the well region to the lifetime of the excited carriers from the confined ground state. If the excited states are in resonance with the top of the barrier potential energy, then the escape time will be greatly reduced, which theoretically minimizes the trapping probability and maximizes the photoconductive gain. Therefore in all of our designs, we attempted to make the energy of the upper excited peak for the main detective peak in resonance with the top of the barrier potential energy.

If  $B\alpha l_{qw} \ll 1$  and  $p_c \ll 1$ , an approximate expression for  $\eta_c$  can be written as

$$\eta_c = A(1 - R) [1 - \exp(-B\alpha l_{qw})] \frac{1 - p_c}{N p_c} \quad (46)$$

$$\approx A(1 - R) \frac{B\alpha l_{qw}}{N p_c}. \quad (47)$$

where  $B$  is a constant dependent on the number of passes the IR radiation makes through the photodetector,  $A$  is a polarization dependent variable equal to 0.5 for n-type QWIPs

and 1 for p-QWIPs,  $R$  is the reflection coefficient,  $l_{qw}$  is the total width of all quantum well regions, and  $\alpha$  is the absorption coefficient.

### 2.2.2.3 Dark Current Relationship in a QWIP

Another important parameter to be considered in a QWIP design is the dark current density ( $J_d$ ), which can be expressed using the Richardson-Dushman equation<sup>14</sup> as

$$J_d \propto T^2 m^* \exp\left(\frac{-\Delta E}{k_B T}\right), \quad (48)$$

where  $m^*$  is the effective mass,  $\Delta E$  is the difference in energy between the barrier height and the quantum confined state in the well,  $k_B$  is the Boltzmann constant, and  $T$  is the temperature. This type of expression assumes that the dominant source of dark current is thermionic emission over the quantum well barrier.

In the low-field regime, the thermionic emission current is related to the density of mobile carriers,  $n_t$  and the average drift velocity,  $v_d$ , and can be expressed as<sup>37</sup>

$$I_{th} = e A_d v_d n_t, \quad (49)$$

where  $A_d$  is the active detector area,  $e$  is the electronic charge, and

$$v_d = \frac{\mu \epsilon}{[1 + (\mu \epsilon / v_s)^2]^{1/2}}, \quad (50)$$

$$n_t = (m^* k_B T / \pi \hbar^2 L) \exp[-(E_{cf} - E_F) / k_B T]. \quad (51)$$

In the above equations,  $\mu$  is the mobility,  $\epsilon$  is the electric field,  $v_s$  is the saturation velocity,  $E_{cf}$  is the cut-off energy related to the cut-off wavelength  $\lambda_c$ , and  $m^* / \pi \hbar^2$  is the two-dimensional density of states. The Fermi energy,  $E_F$ , can be obtained from the expression of  $N_D$ :

$$N_D = \frac{m^* k_B T}{\pi \hbar^2 L} \sum_n \ln \left[ 1 + \exp\left(\frac{E_F - E_n}{k_B T}\right) \right] \quad (52)$$

$$\approx \frac{m^*}{\pi \hbar^2 L} \sum_n (E_F - E_n). \quad (53)$$

Equation (52) for  $N_D$  is valid when summed over the subband levels  $E_n$  below the Fermi level, and Eq. (53) is only valid at cryogenic temperatures.

Using the previous result in the cryogenic temperature regime, we see that the dark current due to thermionic emission is exponentially dependent on the doping concentration in the quantum well, i.e.,

$$I_{th} \propto \exp\left(\frac{E_F}{k_B T}\right) \propto \exp\left(\frac{N_D}{k_B T}\right). \quad (54)$$

Therefore, as the doping density in the quantum well increases, the dark current density due to thermionic emission also increases exponentially. In contrast to this, the intersubband absorption is directly proportional to the doping concentration. Therefore, a tradeoff between the dark current density and the intersubband absorption is required to optimize the QWIP performance. However, in the case of p-QWIPs, the Fermi level in the quantum well is pinned at or slightly above the ground state energy for highly doped quantum wells. We can increase the doping in the quantum well to increase optical absorption without increasing the dark current of the p-QWIP significantly because the thermionic emission is pinned with the Fermi level.

#### 2.2.2.4 Noise in QWIPs

The noise in QWIP structures is mainly due to random fluctuations of thermally excited carriers. The noise is expressed as<sup>5</sup>

$$i_{noise} = \sqrt{4A_d q G \Delta f J_d}, \quad (55)$$

where  $A_d$  is the detector area, and  $\Delta f$  is the bandwidth. Finally, a figure of merit measurement used to compare detectors is the detectivity,  $D^*$ , which is shown to be<sup>19</sup>

$$D^* = \sqrt{A_d \Delta f} \frac{R}{i_{noise}}. \quad (56)$$

If the dark current in a particular QWIP is lower than the 300 K background photocurrent, then the QWIP can be considered to be under background limited performance (BLIP). In a BLIP QWIP, the dominant current is due to photon noise, since all the other sources are negligible by comparison. The photon noise is calculated from the arrival statistics of the incoherent photons. The background photon noise current,  $i_{np}$ , is given by<sup>20,21</sup>

$$i_{np}^2 = 4Aq^2\eta g^2 P_b B_f / (h\nu), \quad (57)$$

where  $P_b$  is the incident background optical power,  $B_f$  is the QWIP bandwidth,  $\eta$  is the absorption quantum efficiency,  $\nu$  is the incident photon frequency, and  $g$  is the noise current

gain. The photocurrent,  $I_p$  can be approximated by

$$I_p = A(q/h\nu)\eta g P_s, \quad (58)$$

where  $P_s$  is the incident optical signal power. The constant,  $A$ , in Eqs. (46), (47), (57), and (58), is due to the polarization selectivity for n-type QWIPs versus p-type QWIPs. As previously stated, for n-type QWIPs,  $A = 0.5$ , while  $A = 1$  for p-type QWIPs. By setting the signal-to-noise power ratio equal to unity, the background limited noise equivalent power,  $(NEP)_{BLIP}$  and the detectivity,  $D_{BLIP}^*$ , for n-type QWIPs can be expressed as

$$(NEP)_{BLIP} = 2\sqrt{2h\nu B P_b / \eta}. \quad (59)$$

$$D_{BLIP}^* = \sqrt{A_d B} / (NEP)_{BLIP} = \frac{\lambda_p}{2\sqrt{2}hc} \left( \frac{\eta}{Q_b} \right)^{1/2}, \quad (60)$$

where  $A_d$  is the active area of the detector, and  $Q_b = P_b / (Ah\nu)$  is the incident photon flux from the background for a given spectral bandwidth,  $\Delta\nu$ , and a peak wavelength,  $\lambda_p$ .  $Q_b$  is defined as

$$Q_b = \frac{2\pi}{c^2} \frac{\nu^2 \Delta\nu}{e^{h\nu/k_B T} - 1} \sin^2 \left( \frac{\theta}{2} \right), \quad (61)$$

where,  $\theta$ , is the field of view (FOV). For a p-type QWIP, a factor of  $\sqrt{2}$  is used in the denominator of Eq. (60),  $D_{BLIP}^*$ , since it can absorb both optical polarizations of the incident IR radiation.

## 2.3 Characterization of Strained Layer P-QWIPs

### 2.3.1 A New p-type InGaAs/GaAs/AlGaAs SBTM QWIP at 10.4 $\mu\text{m}$

A new compressively strained-layer (CSL) p-type QWIP with a detective peak at 10.4  $\mu\text{m}$  based on the InGaAs/GaAs/AlGaAs material system was designed, fabricated, and characterized. The new p-QWIP uses the step-bound-to-miniband (SBTM) intersubband transition as the basis for infrared detection. With this structure, we have again demonstrated the flexibility of the compressively strained p-type QWIP system. This structure exhibits the longest peak wavelength and corresponding cut-off wavelength ( $\geq 13 \mu\text{m}$ ) of any of the p-type QWIPs previously studied, in addition to exhibiting excellent uniformity from device to device.

As illustrated in figure 1, the transition scheme for this p-QWIP is from the ground bound heavy hole state (HH1) to the third excited heavy hole state (HH4), which is in resonance with the miniband formed by the GaAs/Al<sub>0.35</sub>Ga<sub>0.65</sub>As superlattice (SL) barriers. This structure creates a potential difference between the SL barriers and the quantum well which blocks part of the undesirable dark current from the heavily doped ground state in the wide In<sub>0.12</sub>Ga<sub>0.88</sub>As quantum well [41]. The physical parameters described later were chosen so that the ground state in the wide InGaAs quantum well is well above the top of the GaAs/AlGaAs SL barrier, and the third excited heavy-hole state (HH4) is resonant with the ground level of the superlattice miniband (SL1) so that a large quantum well width is maintained for high quantum efficiency, although the absorption coefficient is sacrificed. Along the miniband, the photoexcited holes can easily tunnel due to the large overlap of allowed states in the superlattice barrier at the correct energy, thus transporting through the superlattice barriers until the hole is reabsorbed into a quantum well or collected by the ohmic contacts. The calculated transmission coefficient versus energy is shown in figure 2.

The p-type SBTM CSL-QWIP was grown on a (100) S.I. GaAs substrate by molecular beam epitaxy. It is made up of 90 Å thick quantum wells Be-doped to a density of  $3 \times 10^{18} \text{ cm}^{-3}$ , which populates the ground heavy-hole states (HH1). The quantum well layer is compressively strained with a lattice mismatch of -0.8%. Surrounding the quantum well layers are the superlattice barriers which consist of 20 Å thick superlattice barriers of undoped Al<sub>0.35</sub>Ga<sub>0.65</sub>As alternating with 27 Å thick undoped GaAs superlattice wells. The complete superlattice barrier is then made from ten periods of the alternating superlattice barrier/well structure, which is lattice matched to the GaAs substrate. The whole superlattice barrier/quantum well formations are then repeated 20 times to create the active layers of the p-type SBTM CSL-QWIP. Ohmic contacts are formed from a 0.5 μm thick GaAs cap layer and a 1.0 μm thick GaAs buffer layer, which are heavily Be-doped to  $5 \times 10^{18} \text{ cm}^{-3}$  and are grown on top of the QWIP stack and between the QWIP stack and substrate, respectively. The complete layer structure is given in figure 3.

To facilitate the characterization of the p-QWIP, a  $216 \times 216 \text{ μm}^2$  mesa was etched onto the wafer by wet chemical etching. After patterning with a contact photomask, a thin film of 120 Å of Cr was deposited by e-beam evaporation. This layer was topped off by a 1000 Å thick layer of Au to form both the top and bottom ohmic contacts. The top ohmic contact consists

of a ring-like structure around the edge of the mesa with a  $50 \times 50 \mu\text{m}^2$  contact pad for electrical connection. In this type of contact formation, the normal incidence radiation is only allowed one pass through the QWIP layers; which limits the effective quantum efficiency, especially when compared with those backside illuminated, thinned QWIPs which take advantage of a reflective top layer and waveguide structure to increase the number of times the incident IR radiation passes through the SBTM QWIP.

Device characterization was performed in a closed cycle helium cryogenic dewar. A HP 4145B semiconductor parameter analyzer was used to measure the dark I-V characteristics and the 300 K background photocurrent. Under dark conditions, holes can be transferred out of the quantum wells and produce the thermally generated carriers by two main mechanisms—thermionic emission out of the quantum wells and thermally generated carriers tunneling through the superlattice barriers. Given the high aluminum content in the superlattice barriers (Al fraction is 0.35), a considerable indium content in the quantum well (In fraction is 0.12), and the effect of the compressive strain lowering the energy of the heavy hole states in the quantum well regions, the effective barrier seen by the ground heavy-hole states is 299 meV; which should suppress thermionic emission out of the quantum wells. Because of the heavily doped ohmic contact regions, a large triangle potential is formed which should lower (or thin) the barrier to thermionically assisted tunneling and thus gives rise to a higher than expected dark I-V characteristics. Future designs will take this into account and compensate for the large triangle potential.

Figure 4 shows the measured dark I-V characteristic with the 300 K background photocurrent superimposed. When compared with a similar n-type SBTM QWIP [41], the dark current is much higher. As previously mentioned, the high dark current of this p-QWIP is attributed to the triangle potential formed by the heavily doped ohmic contact, which contributes a large tunneling current component to the dark current.

The measured long-wavelength photoresponse for the p-type SBTM CSL-QWIP is shown in figure 5. A single peak was found at  $\lambda_p = 10.4 \mu\text{m}$ , which is in excellent agreement with the theoretically calculated value of  $10 \mu\text{m}$ . With a long wavelength cut-off,  $\lambda_c \geq 13 \mu\text{m}$ , and a half-peak value at  $12 \mu\text{m}$ , we determined the spectral bandwidth to be,  $\Delta\lambda/\lambda_p = 20 \%$ . This narrow responsivity bandwidth is consistent with that expected from a bound-to-miniband transition scheme. The maximum responsivity of  $28 \text{ mA/W}$  was found at  $T=65$

K and  $V_b = +3.0$  V, as seen in figure 6, the responsivity versus bias curve. As seen in the  $T = 40$  K curve, the gain of the p-type SBTM CSL-QWIP has not saturated at  $V = 5.0$  V. The apparent saturation of the photoresponse of the  $T = 65$  K curve is due to the limitations of our amplifiers. At  $T = 65$  K, the noise spectral density was estimated as  $4.0 \times 10^{-26} \text{ A}^2/\text{Hz}$  at a bias of 1.0 V. Corresponding to this operating point, the measured responsivity at  $10.4 \mu\text{m}$  was  $13 \text{ mA/W}$ . Using the above data, the spectral detectivity was determined to be  $D^* = 1.4 \times 10^9 \text{ cm}\sqrt{\text{Hz}}/\text{W}$ .

### 2.3.2 Noise Performance of a p-type Strained-layer QWIPs

The noise performance of the  $7.4 \mu\text{m}$  peak ultra-low dark current p-QWIP was extensively studied during this reporting period. The performance specifications of this p-QWIP are summarized in Table 1 and are explained in detail in the previous report.

Measurements were carried out using standard noise measurement procedures [38]. A Brookdeal 5004 low noise amplifier (LNA) which has an input referred current noise,  $S_{in} \approx 4 \times 10^{-27} \text{ A}^2/\text{Hz}$ , was used to amplify the signal generated by the device. Since this detector exhibits very low current noise and high dynamic resistance, we were limited by the amplifier current noise. The spectral density of the output of the LNA was measured using a HP 3561A spectrum analyzer. The device was placed in a nitrogen flow cryostat which allows for temperature variation between 80 K and room temperature. The cryostat also acted as an external noise shield.

Figure 7 shows the noise spectra measured from 10 Hz to 100 kHz. In the high frequency range ( $f > 1 \text{ kHz}$ ), the noise spectral density is affected by RC parasitic effects. But after corrections are made, frequency independent noise levels are found. The noise plateaus are attributed to hole trapping and detrapping in the quantum well bound states. The data also indicates that most of the current spectra are frequency independent down to 10 Hz. Only under high bias, e.g.  $|V_{bias}| > 4 \text{ V}$ , does excess noise show up in the spectra for frequencies below 100 Hz.

The noise plateau values plotted as a function of dark current is shown in Figure 8. From this plot, two distinct regimes of operation can be recognized. In the low field diffusion dominant regime, noise values are nearly independent of the DC current. The observed low bias noise values agree with those calculated from the Nyquist expression at zero applied



bias voltage for the measured temperatures. In the high field, drift dominated regime, the noise values become strongly dependent on the DC current. This general behavior is quite similar to what Rose predicted for traditional photoconductive devices [42].

From the measured data, we were able to determine the expression for the noise current plateau values in the drift dominant regime as

$$S_i = \frac{4I_d^2}{NAL_w C e^{(-\frac{E_b - \Delta E}{k_B T})}}, \quad (62)$$

where  $I_d$  is the dark current,  $N$  is the total number of quantum wells,  $A$  is the device cross-sectional area,  $L_w$  is the width of the quantum well,  $E_b = E_v - E_o$  is the energy barrier seen by the holes in the quantum well states,  $\Delta E = q\Delta\phi + q\varepsilon L_w$ , which is the total energy barrier lowering including both the electric field effect and the Schottky image effect,  $k_b$  is the Boltzmann constant,  $T$  is the temperature, and  $C$  is the hole generation rate constant.  $C$  was determined to be  $9.4 \times 10^{30} \text{ cm}^{-3}\text{s}^{-1}$ , by fitting measured data with the above equation. Using this data and the expression for the noise current spectral density in the diffusion dominated regime,

$$S_i = 4q^2 N A L_w C e^{(-\frac{E_b - \Delta E}{k_B T})} \left( \frac{L_D}{L} \right)^2, \quad (63)$$

we can determine the diffusion length,  $L_D$ . For this device, the diffusion length was found to be 450 Å.

The following model is used to explain the value of  $C$  and derive a value for the capture cross section  $\sigma_p$  within the context of the hole transport mechanism and quantum well characteristics. Thermally generated heavy holes will move via drift or diffusion in the barrier region to a neighboring quantum well. These quantum wells are heavily doped with beryllium acceptors to a concentration of  $2 \times 10^{18} \text{ cm}^{-3}$ , which results in an inter-acceptor spacing of about 100 Å. Since the well width is only 48 Å, these acceptors are postulated to basically form a thin plane of nearly neutral charge centers. The holes approaching this monolayer with a thermal velocity determined by barrier parameters will interact with these Be-centers, triggering a recombination process. Assuming ineffective screening of the Be nuclei due to the two dimensionality of the surrounding electron gas, the Be perturbation potential can be approximated by  $\frac{Zq}{4\pi\epsilon_0\epsilon_r r}$ , where  $Z=4$  [43]. Note that holes impinging on the Be-centers gain kinetic energy by crossing the barrier/quantum well interface. Thus the perturbation potential must equal the energy gained from the barrier/quantum well interface

and the hole thermal energy, or

$$\frac{Zq}{4\pi\epsilon_o\epsilon_r r} = E_b + E_{th}, \quad (64)$$

from which  $\sigma_p = \pi r^2$  can be calculated.

We calculated at  $T=100$  K, that  $\sigma_p(100 \text{ K}) = 1.9 \times 10^{-13} \text{ cm}^2$ . The measured value that follows from  $C = N_a N_v v_{th} \sigma_p = 9.4 \times 10^{30} \text{ cm}^{-3} \text{ s}^{-1}$ . Using  $N_a = 2 \times 10^{18} \text{ cm}^{-3}$  and bulk GaAs values for  $N_v$  and  $v_{th}$ , we find that  $\sigma_{p,exp} = 2.6 \times 10^{-13} \text{ cm}^2$ , which is in good agreement with the predictions of this model.

At zero bias, the following picture emerges for QWIP operation. Holes are thermally generated from the quantum well bound states into the extended states of the device with equal probabilities for transferring to the neighboring quantum well on the anode or cathode side, in equilibrium. The hole lifetime of the bound states is large compared to the barrier transit time, allowing the holes to fully thermalize in the wells. This thermalization process decouples the statistical fluctuations in hole transport through a barrier from one period to the next. As a result, the QWIP can be thought of as consisting of  $N$  statistically independent sections made up of a barrier region with two contacts from which the holes are emitted. In equilibrium, the net hole current through any cross sectional plane is zero, which results from the detailed balance between two opposing currents,  $I_o$ . Assuming full shot noise in each current, the current noise spectral density of a single section becomes  $S_{i(section)} = 4qI_o$ . Then the total noise is

$$S_i = \frac{S_{i(section)}}{N} = \frac{4qI_o}{N} = S_{i(Nyquist)}. \quad (65)$$

When an electric field is present, producing a voltage drop,  $V_b$  across a section, then the total current becomes

$$I = I_s [1 - \exp(-\frac{qV_b}{k_B T})] \quad (66)$$

where  $I_s$  is the saturation current. In equilibrium,  $I_s = I_o$  and the total current is zero. With an electric field, the saturation current will increase due to field induced barrier lowering and the image effect. So that,  $I_s = I_o \exp(\frac{\Delta E}{k_B T})$ , and the dark current values can be calculated. The measured dark current and our calculated results based on the above equations are shown in figure 9.

We also measured and modelled the dark I-V characteristics of a InGaAs/AlGaAs p-type QWIP with a detection peak at  $9.2 \mu\text{m}$ . A detailed summary of this device can be

found in the previous report, and a brief outline of the device characteristics are given in table 1.

Figure 10 shows the dark I-V characteristics of this 9.2  $\mu\text{m}$  peak p-QWIP. The current was calculated assuming a constant applied electric field throughout the device, and at low fields, the holes are thermally generated from a quantum well and travel, on average, one period before they trap and fully thermalize into the neighboring quantum wells. As seen, good agreement is obtained between the theoretical calculations (symbols) and the measured results (solid line).

## 2.4 Conclusion and Remarks

During this reporting period, we have achieved a better understanding in regards to the design and characterization of P-QWIPs. We previously demonstrated a novel strained-layer design that utilizes biaxial tension on an InP substrate with ultra-low dark current, high detectivity, high responsivity, and BLIP operation. We have also demonstrated a reliable, novel compressively strained-layer designs on a GaAs substrate with detective peaks at 7.4, 8.4, 8.9, 9.2, and 10.1  $\mu\text{m}$  in the LWIR band and 5.5  $\mu\text{m}$  in the MWIR band with high detectivity, high responsivity, and high gain. We have demonstrated detectivities of  $4.0 \times 10^9$ ,  $1.66 \times 10^{10}$ ,  $2.7 \times 10^9$ , and  $1.04 \times 10^9 \text{ cm}\sqrt{\text{Hz}}/\text{W}$  with the 8.9, 7.4, 9.2, 10.1  $\mu\text{m}$  peak wavelength p-QWIPs. We are currently pursuing the application of p-type QWIPs with step bound-to-miniband transition schemes in an effort to lower dark current and noise levels while maintaining normal incidence detection and responsivity. The current p-type SBTM CSL-QWIPs exhibit a LWIR detection peak at 10.4  $\mu\text{m}$  with a corresponding  $D^* = 1.4 \times 10^9 \text{ cm}\sqrt{\text{Hz}}/\text{W}$  at  $T=65 \text{ K}$  and  $V=1 \text{ V}$ . Efforts are currently underway to lower the dark current of the SBTM p-QWIPs even further for higher temperature operation, including barriers that limit the effect of the large triangle potential of the ohmic contacts. A study of the effects of strained quantum wells towards actual responsivity is also underway. These devices have been grown and will be fabricated and characterized for the next reporting period. Additional headway has been made in the modeling of the dark current characteristics of the 9.2 and 7.4  $\mu\text{m}$  peak compressively strained p-QWIPs, along with the analysis of the noise performance of the 7.4  $\mu\text{m}$  peak p-type compressively strained p-QWIP.

## References

1. B. F. Levine, R. J. Malik, J. Walker, K. K. Choi, C. G. Bethea, D. A. Kleinman, and J. M. Vandenberg, *Appl. Phys. Lett.* **50**, 273 (1987).
2. L. S. Yu, S. S. Li, *Appl. Phys. Lett.* **59**, 1332 (1991).
3. G. Hasnain, B. F. Levine, C. G. Bethea, R. A. Logan, J. Walker, and R. J. Malik, *Appl. Phys. Lett.* **54**, 2515 (1989).
4. J. Y. Andersson and L. Lundqvist, *J. Appl. Phys.* **71**, 3600 (1992).
5. B. F. Levine, S. D. Gunapala, J. M. Kuo, S. S. Pei, and S. Hui, *Appl. Phys. Lett.* **59**, 1864 (1991).
6. J. Katz, Y. Zhang, and W. I. Wang, *Electron. Lett.* **28**, 932 (1992).
7. W. S. Hobson, A. Zussman, B. F. Levine, and J. deJong, *J. Appl. Phys.* **71**, 3642 (1992).
8. J. W. Matthews and A. E. Blakeslee, *J. Cryst. Growth* **32**, 265 (1976).
9. Landolt-Börnstein, "Numerical Data and Functional Relationships in Science and Technology", O. Madelung, ed., Group III, **17a**, **22a**, Springer-Verlag, Berlin (1986).
10. G. Ji, D. Huang, U. K. Reddy, T. S. Henderson, R. Houre, and H. Morkoç, *J. Appl. Phys.* **62**, 3366 (1987).
11. T. P. Pearsall, *Semiconductors and Semimetals*, **32**, 55 (1990).
12. H. Asai, and Y. Kawamura, *Appl. Phys. Lett.* **56**, 746 (1990).
13. H. Xie, J. Katz, and W. I. Wang, *Appl. Phys. Lett.* **59**, 3601 (1991).
14. R. T. Kuroda and E. Garmire, *Infrared Phys.* **34**, 153 (1993).
15. L. R. Ram-Mohan, K. H. Yoo, and R. L. Aggarwal, *Phys. Rev B* **38**, 6151 (1988).
16. J. M. Luttinger and W. Kohn, *Phys. Rev.* **97**, 869 (1956).

17. J. M. Luttinger, Phys. Rev. **102**, 1030 (1956).
18. G. L. Bir and G. E. Pikus, "Symmetry and Strain-Induced effects in Semiconductors", Wiley, New York (1974).
19. E. L. Derniak and D. G. Crowe, Optical Radiation Detectors, Wiley, New York (1984).
20. B. F. Levine, C. G. Bethea, G. Hasnain, J. Walker, and R. J. Malik, Appl. Phys. Lett. **53**, 296 (1988).
21. D. A. Scribner, M. R. Kruer, and J. M. Killiany, Proc. of the IEEE **79**, 66, (1991).
22. R. Hull, J. C. Bean, F. Cerdeira, A. T. Fiory, and J. M. Gibson, Appl. Phys. Lett. **48**, 56 (1986).
23. E. O. Kane, "Semiconductors and Semimetals", eds. R. K. Willardson and A. C. Bear, **1**, 75 (1966).
24. F. H. Pollack, "Semiconductors and Semimetals", ed. T. P. Pearsall, **32**, 17 (1990).
25. Y. C. Chang and R. B. James, Phys Rev. **B-39**, 672 (1989).
26. P. Man and D. S. Pan, Appl. Phys. Lett. **61**, 2799 (1992).
27. S. K. Chun, D. S. Pan, and K. L. Wang, Phys. Rev. **B-47**, 15638 (1993).
28. B. F. Levine, J. Appl. Phys. **74**, R1 (1993).
29. J. W. Matthews and A. E. Blakeslee, J. Cryst. Growth **27**, 118 (1974).
30. J. W. Matthews and A. E. Blakeslee, J. Cryst. Growth **29**, 273 (1975).
31. K. Hirose, T. Mizutani, and K. Nishi, J. Cryst. Growth **81**, 130 (1987).
32. H. C. Liu, Z. R. Wasilewski, and M. Buchanan, Appl. Phys. Lett. **63**, 761 (1993).
33. A. K. Ghatak, K. Thyagarajan, and M. R. Shenoy, IEEE J. Quantum Electron. **24**, 1524 (1988).
34. H. C. Liu, Appl. Phys. Lett. **60**, 1507 (1992).

35. H. C. Liu, Appl. Phys. Lett. **61**, 2703 (1992).
36. W. A. Beck, Appl. Phys. Lett. **63**, 3589 (1993).
37. S. D. Gunapala, B. F. Levine, and K. West, J. Appl. Phys. **69**, 6517 (1991).
38. D. C. Wang, G. Bosman, Y. H. Wang, and S. S. Li, J. Appl. Phys. **77**, 1107 (1995).
39. Y. H. Wang, S. S. Li, J. Chu, and Pin Ho, Appl. Phys. Letts., **64**, 727 (1994).
40. Y. H. Wang, J. C. Chiang, and S. S. Li, and Pin Ho, J. Appl. Phys. **76**, 2538 (1994).
41. L. S. Yu, Y. H. Wang, and S. S. Li, Appl. Phys. Lett. **60** (8), 992 (1992).
42. A. Rose, "Concepts in Photoconductivity and Allied Problems", Wiley-Interscience, New York, 1963.
43. R. H. Bube, "Electronic Properties of Crystalline Solids", Academic Press, New York, 1974.

<i>Device</i> (strain)	$\lambda_p$ ( $\mu\text{m}$ )	<i>Responsivity</i> (mA/W)	<i>Dark Current Density</i> (A/cm <sup>2</sup> ) @ 77 K, 1 V
InGaAs/InAlAs (tensile)	8.1	18	$5 \times 10^{-8}$
InGaAs/GaAs (compressive)	8.9, 8.4, 5.5	45	$2.5 \times 10^{-2}$
InGaAs/AlGaAs (compressive)	7.4, 5.5	38	$1.1 \times 10^{-4}$
InGaAs/AlGaAs (compressive)	9.2	28	$1.6 \times 10^{-2}$
InGaAs/AlGaAs (compressive)	10.1	17	$5 \times 10^{-2}$
InGaAs/GaAs/AlGaAs (compressive)	10.4	25	$4 \times 10^{-2}$

**Table 1.** Comparison of the strained layer p-QWIPs studied so far.

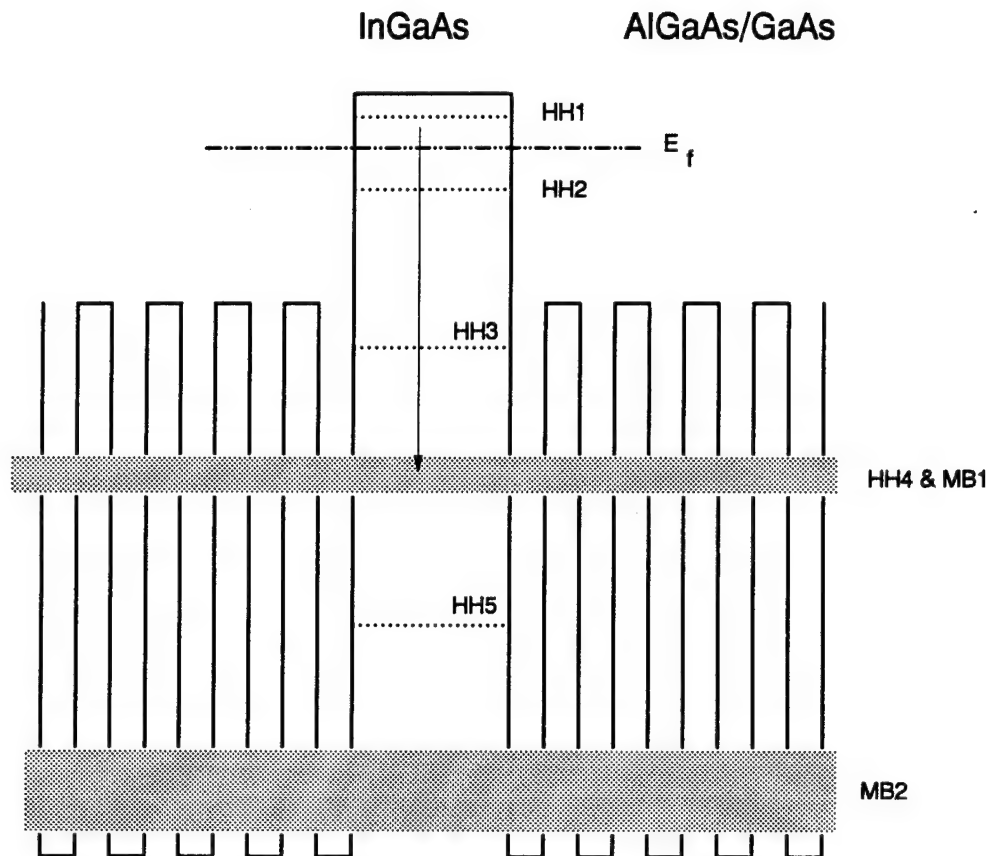


**Figure 1:** The schematic diagram for new 10.4  $\mu\text{m}$  peak compressively strained InGaAs/AlGaAs/GaAs p-type SBTM CSL-QWIP.



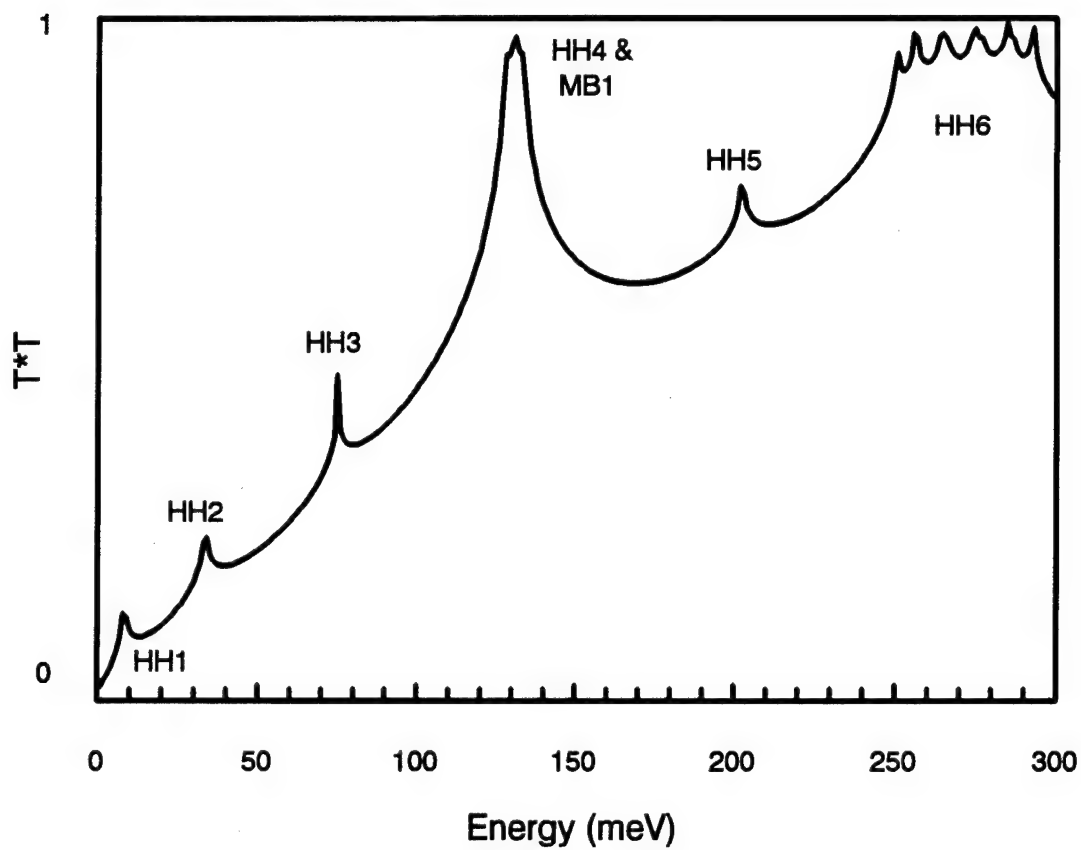


**Figure 2:** The calculated transmission peaks for the InGaAs/AlGaAs/GaAs compressively strained p-type SBTM CSL-QWIP.

	0.5 $\mu\text{m}$	GaAs	$p=5\times 10^{18} \text{ cm}^{-3}$	
20 $\times$	{	20 $\text{\AA}$	$\text{Al}_{0.35}\text{Ga}_{0.65}\text{As}$	undoped
		27 $\text{\AA}$	GaAs	undoped
		$\vdots$		
		90 $\text{\AA}$	$\text{In}_{0.12}\text{Ga}_{0.88}\text{As}$	$p=3\times 10^{18} \text{ cm}^{-3}$
		$\vdots$		
	20 $\text{\AA}$	$\text{Al}_{0.35}\text{Ga}_{0.65}\text{As}$	undoped	} $\times 10$
	27 $\text{\AA}$	GaAs	undoped	
	$\vdots$			
	1.0 $\mu\text{m}$	GaAs	$p=5\times 10^{18} \text{ cm}^{-3}$	
SI (100) GaAs				

**Figure 3:** The layer structure for the p-type SBTM CSL-QWIP.

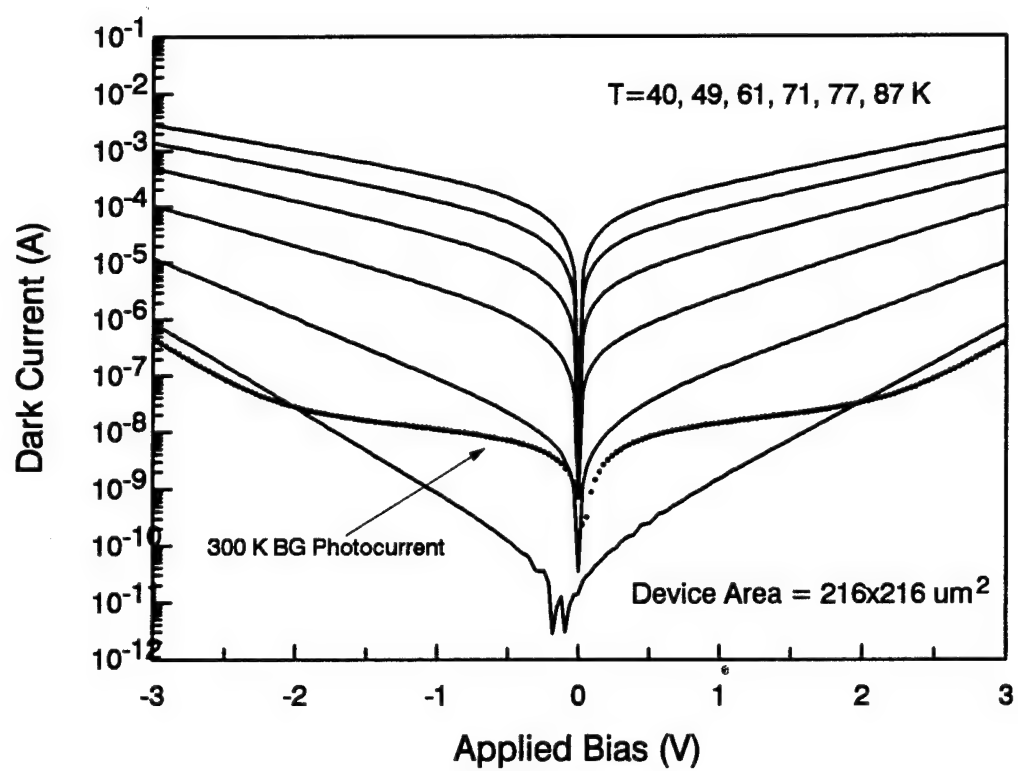


**Figure 4:** Measured dark I-V and 300 K background photocurrents for the p-type SBTM CSL-QWIP.

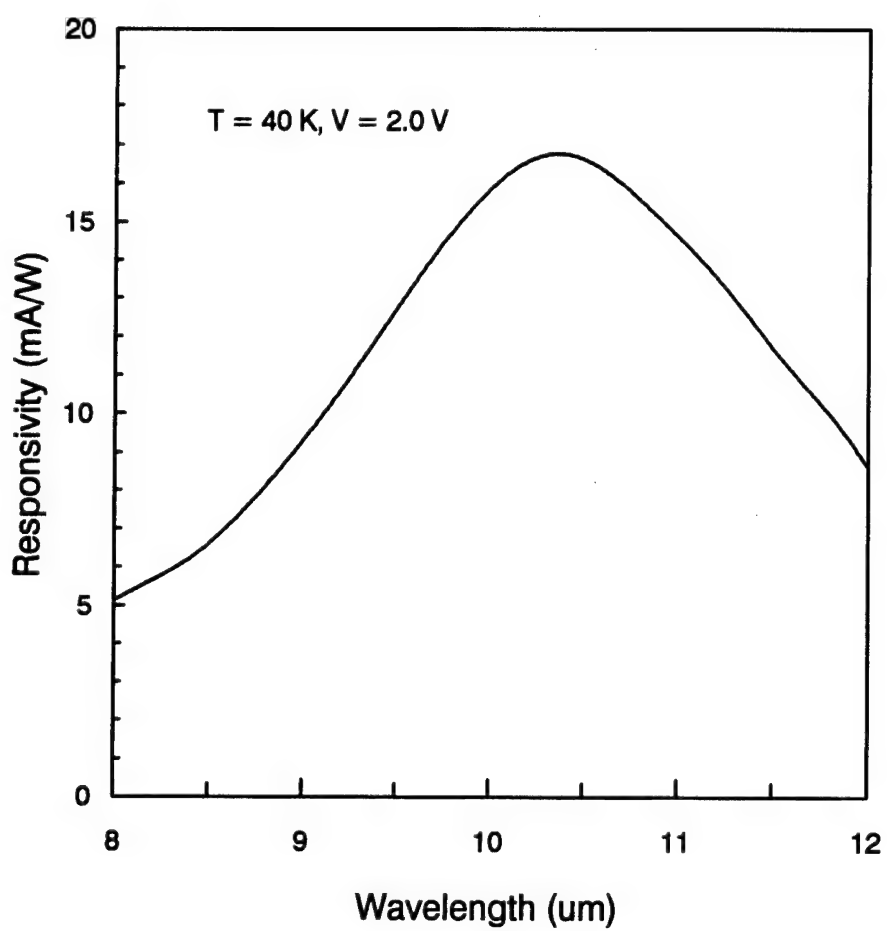


**Figure 5:** The measured photoresponse versus incident IR wavelength at  $T=60$  K,  $V=2.0$  V for the p-type SBTM CSL-QWIP.

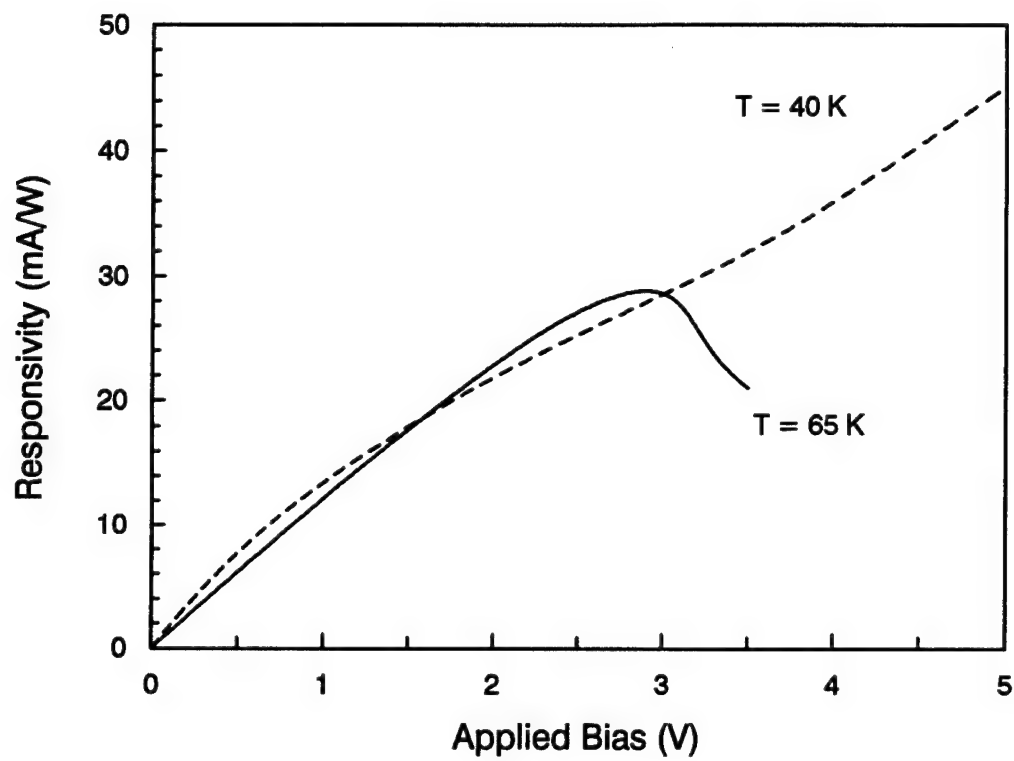


**Figure 6:** The measured responsivity versus bias at  $10.4 \mu\text{m}$  and various temperatures.

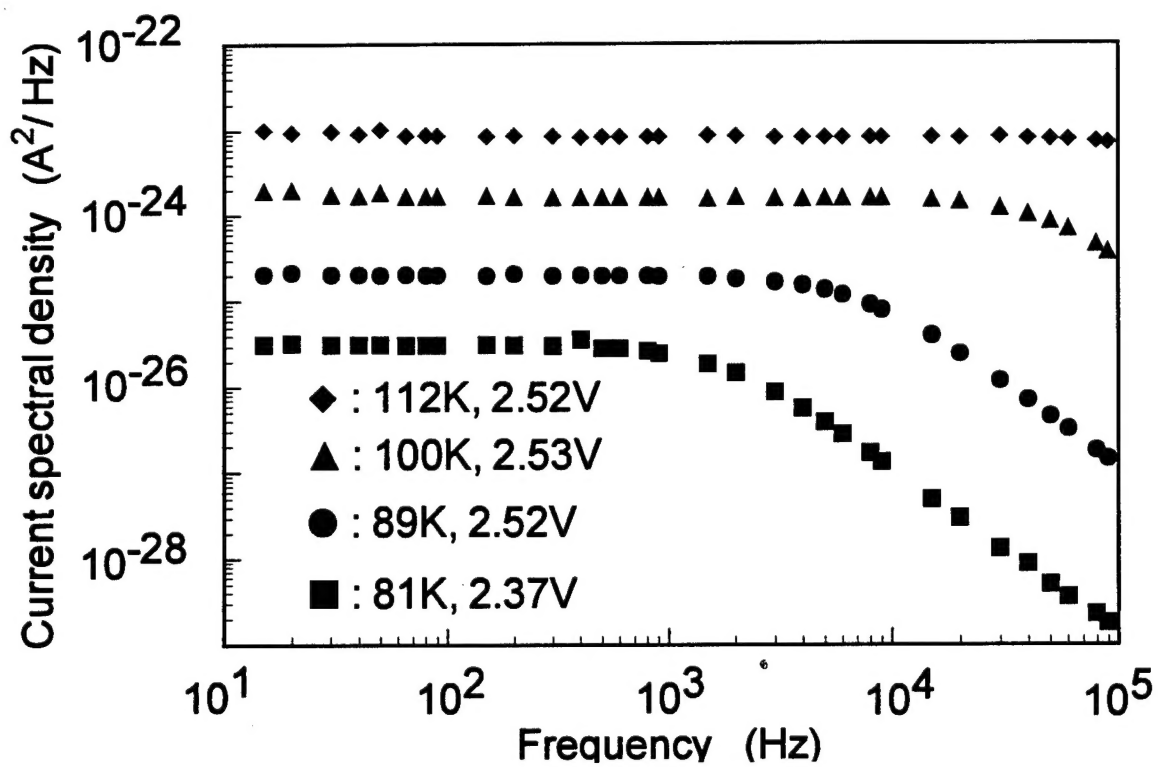


**Figure 7:** Current noise spectral density versus frequency at different bias voltages and temperatures.

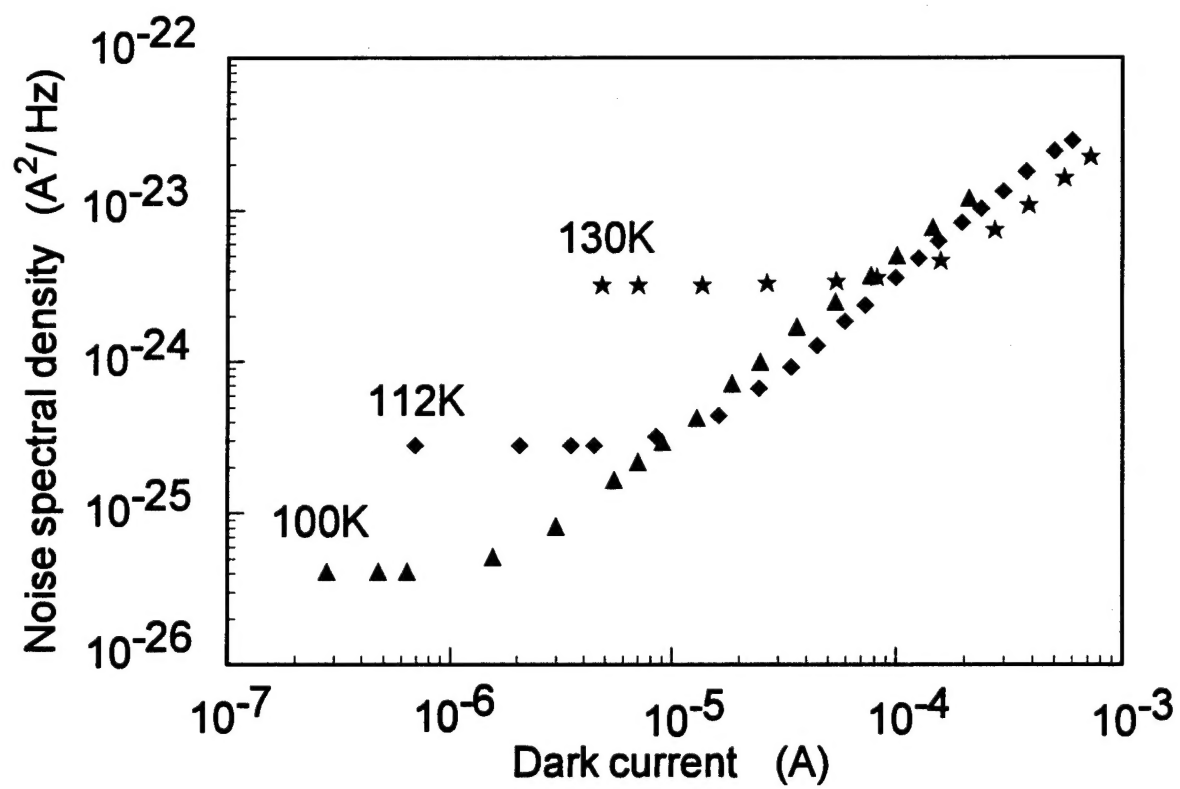


**Figure 8:** Current noise spectral density versus dark current for various temperatures.

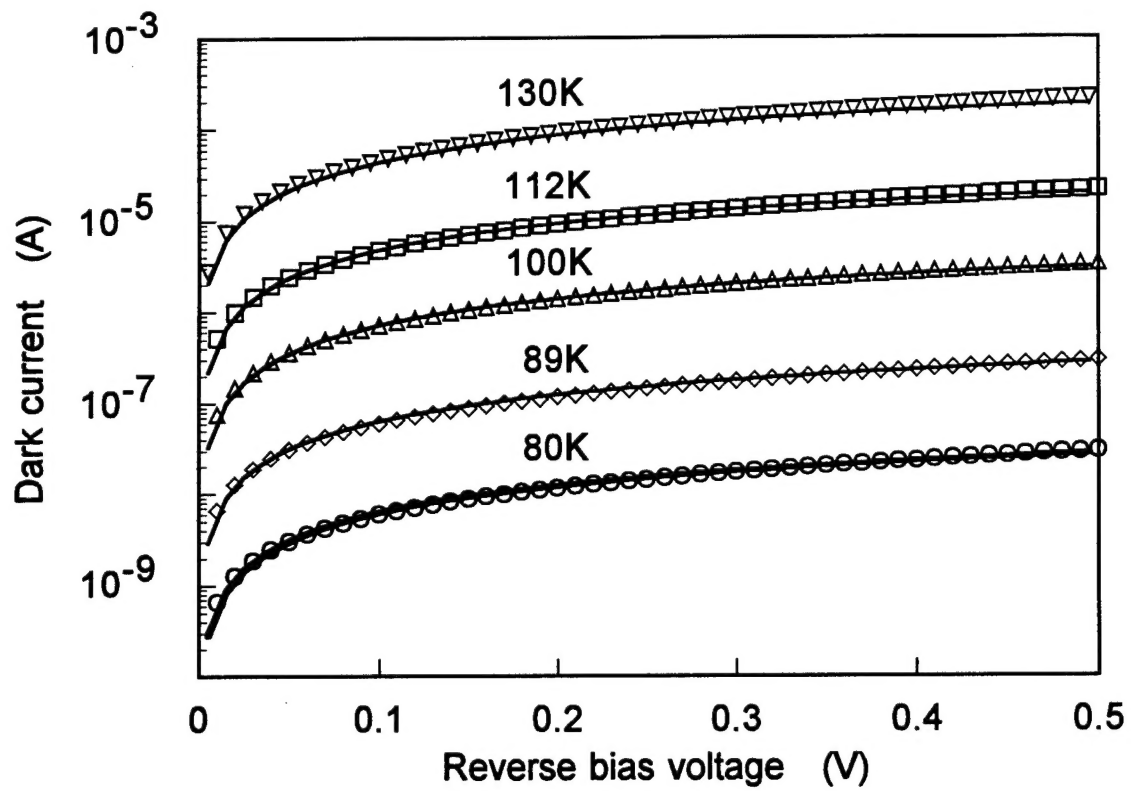


**Figure 9:** Measured and calculated dark currents of the 7.4  $\mu\text{m}$  peak InGaAs/AlGaAs at low bias voltages and different temperatures.



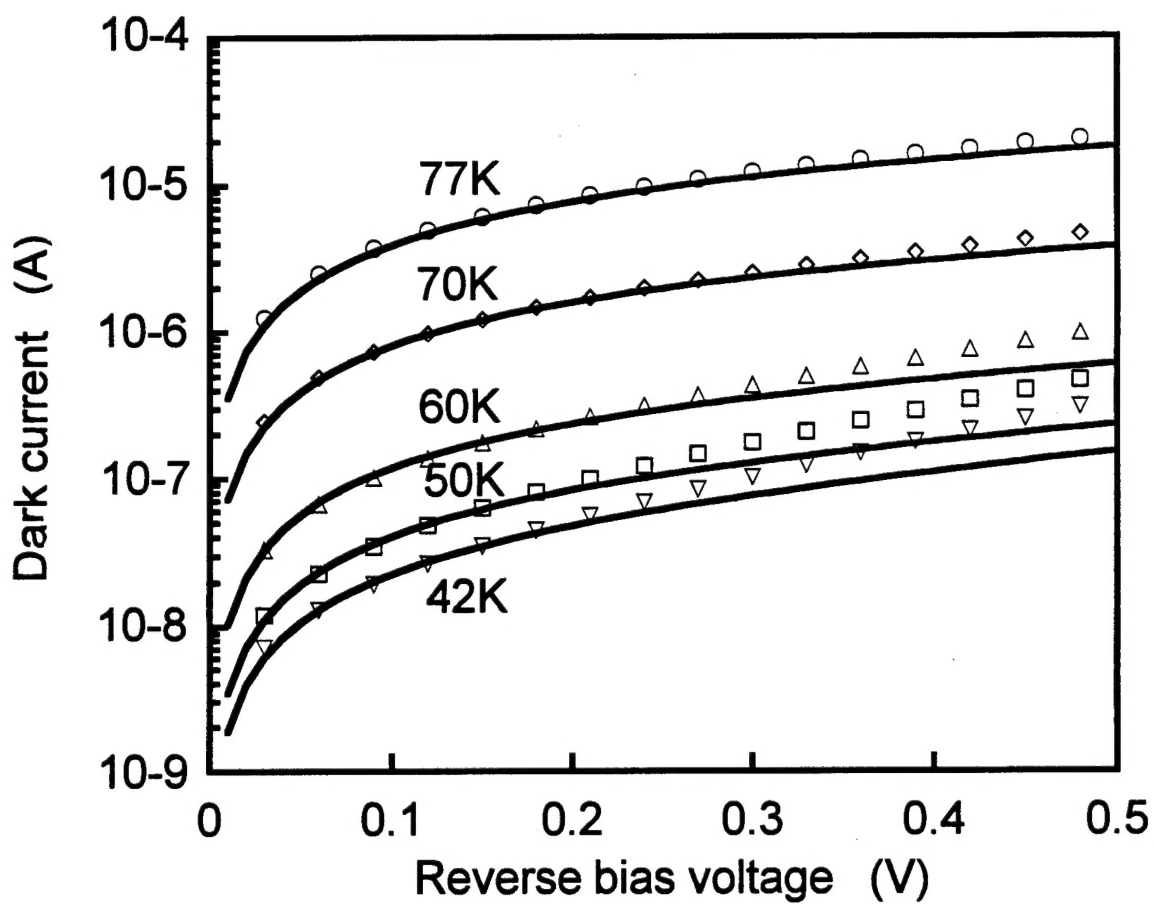


**Figure 10:** Measured and calculated dark current of the 9.2  $\mu\text{m}$  peak p-QWIP at low applied biases and various temperatures.